E.V. Kravchenko
Astro Space Center of Lebedev Physical Institute

ASTRO SPACE CENTER

Radio and gamma-ray study of the quasar S4 1030+611 during its activity in 2009-2014

We present a detailed study of the parsec-scale multi-frequency properties of the quasar S4 1030+61 during a prolonged radio and gamma-ray activity in the period of 2009--2014. Observations were performed by the Fermi Gamma-ray Space Telescope, VLBA and OVRO 40-m telescope covering five years starting from 2009. Observations cover a strong gamma-ray flare in the source accompanied by a high radio activity and observed emergence of a new parsec-scale jet component. Analysis shows that the radio flaring activity of the quasar results from an injection of relativistic particles and energy losses at the jet base, where gamma-ray emission originates, while S4 1030+61 has stable, straight jet well described by standard conical jet theories.

Observations

2010 – 2011   4 epochs of VLBA observations at 4.6, 5.0, 8.1, 8.4, 23.8, 43.2 GHz (2010–05–24, 2010–07–09, 2010–08–28, 2010–10–18)
2009 – 2013   15 GHz monitoring within VLBA MOJAVE program (10 epochs)
2008 – 2014   *Fermi*-LAT (E = 0.1-200 GeV) monitoring
2008 – 2014   monitoring at 15GHz at 40-m Radio Telescope of the Owens Valley Radio Observatory (OVRO)
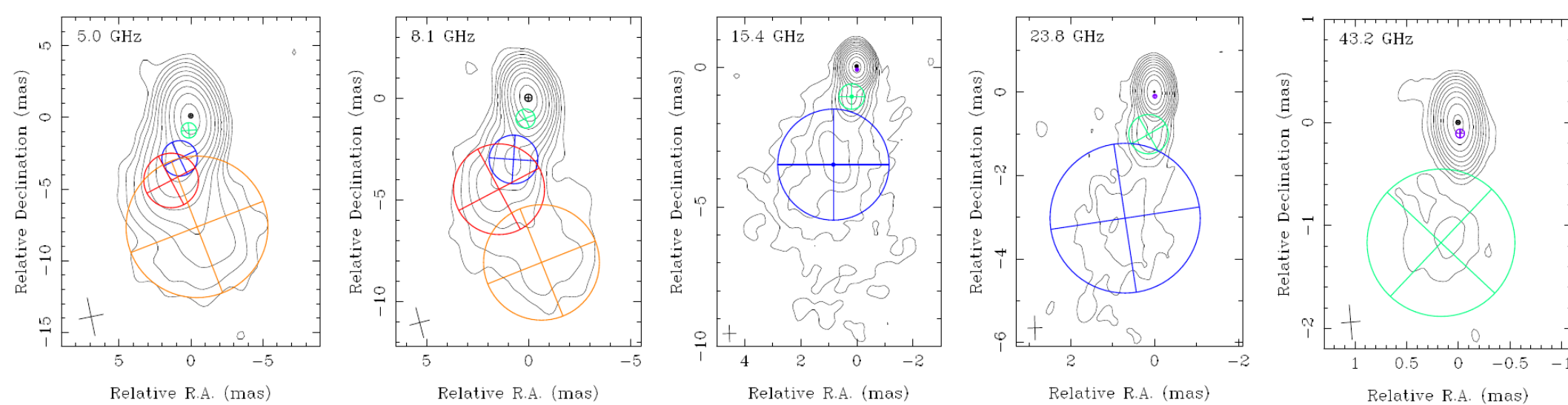
Kinematics and Structure

Figure 1. Stacked naturally weighted contour images of total intensity over four multi-wavelength epochs at 5.0, 8.1, 15.4, 23.8 and 43.2 GHz (from left to right). Contours of equal intensity are plotted starting from 3 rms level and increase in factors of 2. The 1 rms value equals to 0.07, 0.07, 0.14, 0.10 and 0.23 mJy at 5.0, 8.1, 15.4, 23.8 and 43.2 GHz respectively. The full width at half maximum of the synthesized beam is shown in the bottom left corner of every image. Color circles represent model-fit components.

The structure of the source is modeled by a number of 2D Gaussian components in the *uv*-plane, and sown in Figure 1. Three components (Core, C2 and C3) find consistent cross-identification through all frequencies. Assuming position of the core to be stationary in time, apparent speeds and ejection epochs of the components were estimated and shown in Figure 2 and Table 1.

Spectral index of the core region sows inverted spectrum and evolves in time from 0.47±0.02 at 2010–05–24 to 0.69±0.02 at 2010–10–18 as flare rises.
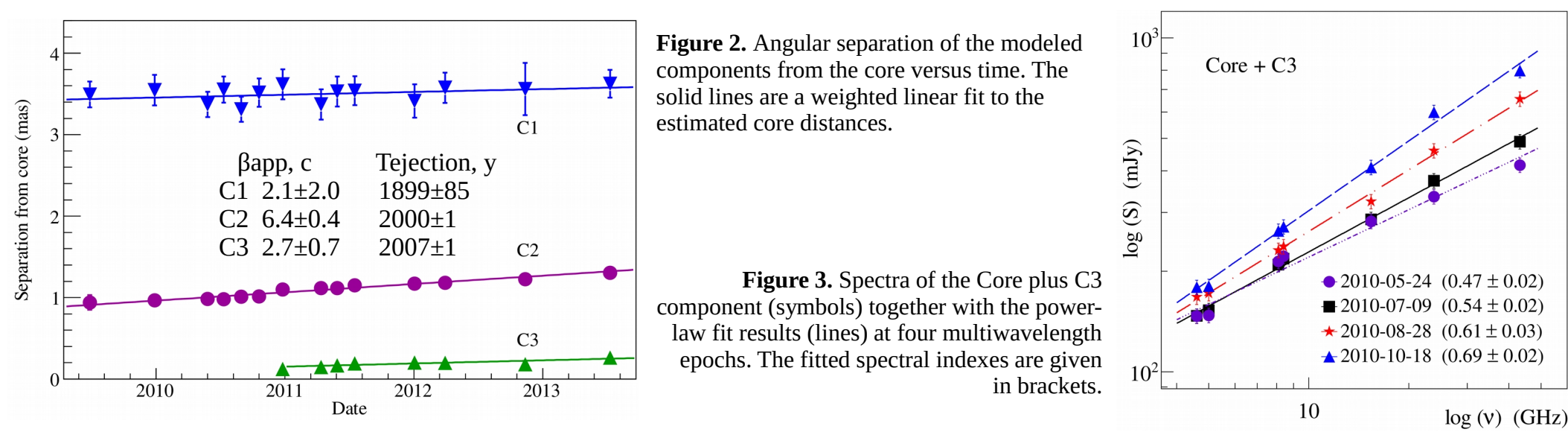
Figure 2. Angular separation of the modeled components from the core versus time. The solid lines are a weighted linear fit to the estimated core distances.

	β_{app}, c	Tejection, y
C1	2.1±2.0	1899±85
C2	6.4±0.4	2000±1
C3	2.7±0.7	2007±1

Figure 3. Spectra of the Core plus C3 component (symbols) together with the power-law fit results (lines) at four multiwavelength epochs. The fitted spectral indexes are given in brackets.

Core + C3

- 2010-05-24 (0.47 ± 0.02)
- 2010-07-09 (0.54 ± 0.02)
- 2010-08-28 (0.61 ± 0.03)
- 2010-10-18 (0.69 ± 0.02)

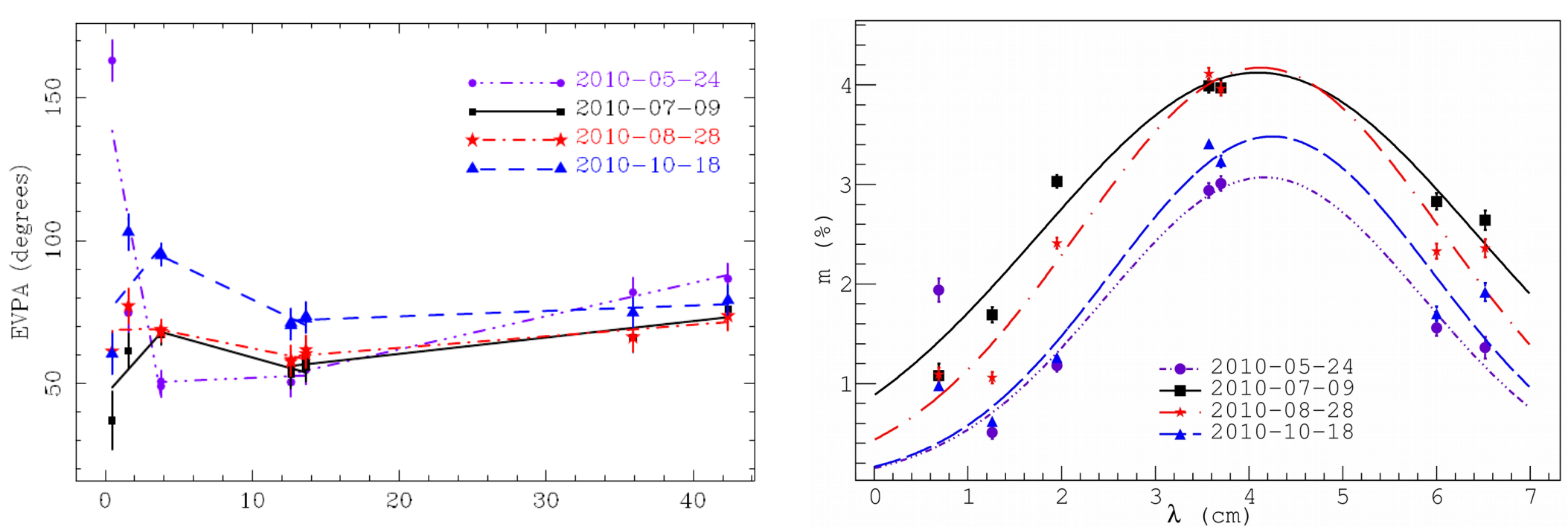## Linear Polarization and Faraday effects

Figure 4. Electric vector position angle at the central pixel of the image (points) versus squared wavelength and fitted Faraday rotation (lines) at four epochs.

- 2010-05-24
- 2010-07-09
- 2010-08-28
- 2010-10-18

Figure 5. Degree of polarization vs. wavelength in the core region at four epochs. Results of a Gaussian fit to the data points are shown.

- 2010-05-24
- 2010-07-09
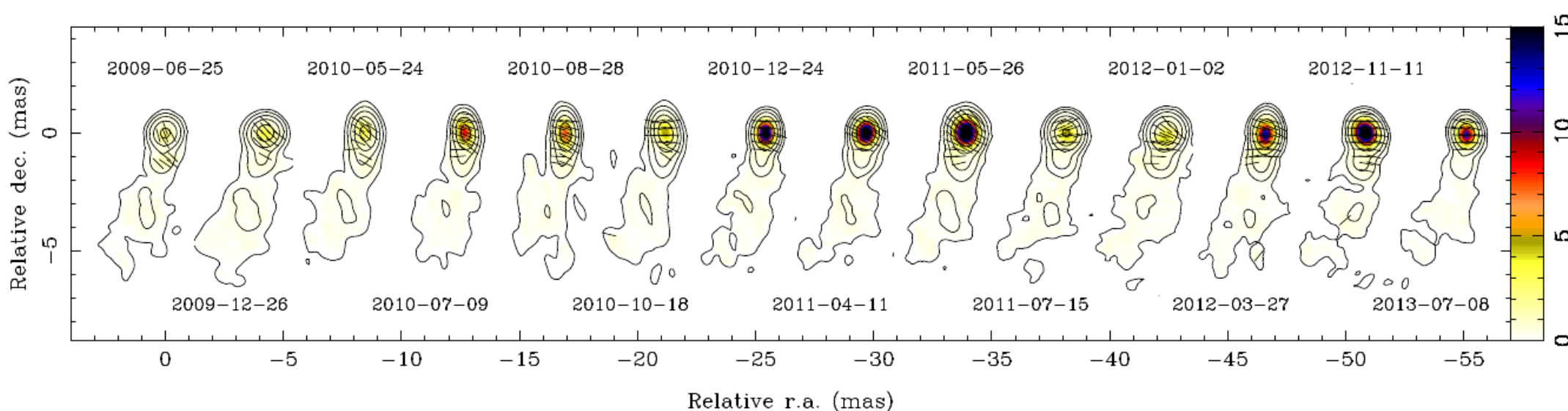- 2010-08-28
- 2010-10-18

Figure 6. S4 1030+61 naturally weighted contour images of total intensity at 15 GHz from 2009 (left) to 2013 (right) for all the MOJAVE epochs. Contours of equal intensity are plotted starting from 4 r.m.s. level at x5 steps. The average Electric Vector Position Angle (EVPA) uncertainty is ±5 degrees. The overlaid color images show the linearly polarized intensity in mJy, and ticks represent the direction of EVPA, not corrected for Faraday effects.

The core region of the source is strongly affected by Faraday effects (see Figure 4 and Figure 5 for EVPA-λ^2 and degree of polarization - λ dependences). Possible explanations for such behavior are the following: (i) anomalous or inverse depolarization, which appears in a regular twisted or tangled magnetic fields; (ii) spectral depolarization due to smearing of multiple components within the observed region. The EVPA vs. λ^2 behavior is consistent with both hypotheses.

43 GHz EVPA maps, which are less sensitive to Faraday effects, show longitudinal direction of the magnetic field in the core region. Electric vectors maps at 15 GHz, uncorrected for RM, are shown in Figure 6, and show small variations of the EVPA from transversal direction relative to the jet direction. Both the linearly polarized flux density and the degree of linear polarization at 15 GHz do not show correlation with the total flux density.

Apparent Core Shift

Study of the apparent frequency-dependent shift of the radio core position, r_c, is done with the 2D cross-correlation method. Because of (i) ongoing flaring activity, (ii) low flux density in the extended jet component of the source at high frequencies, and (iii) blending of the core with the newly-born component, reliable results of the core shift have been obtained only at two epochs (see Figure 7) and follow $r_c \propto v^{-k}$, where k is fixed to 1.

This leads to the deprojected distance of the apparent radio core from the central black hole of (14±3) pc.

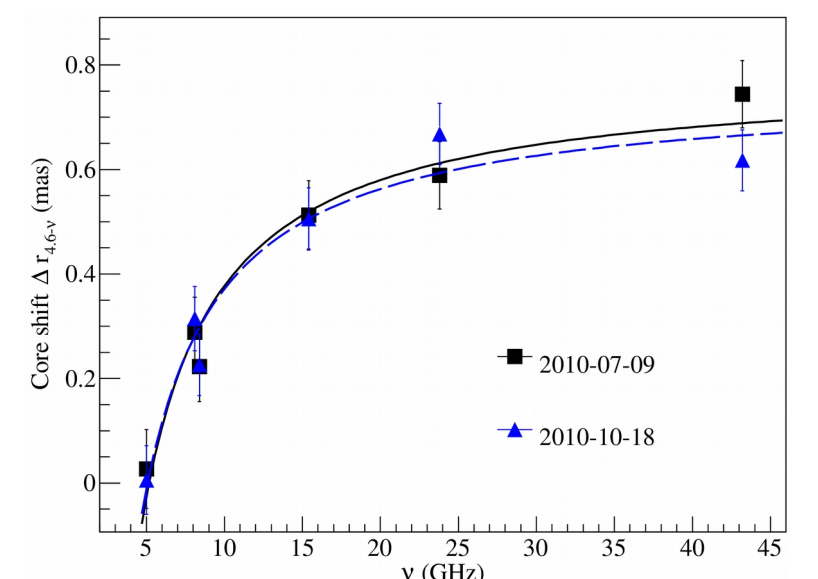**Figure 7.** Measured value of the core shift relative to 4.6 GHz at two selected epochs. The curves represent a fit to the function $a^{-1}+b$ (solving for a and b).

- 2010-07-09
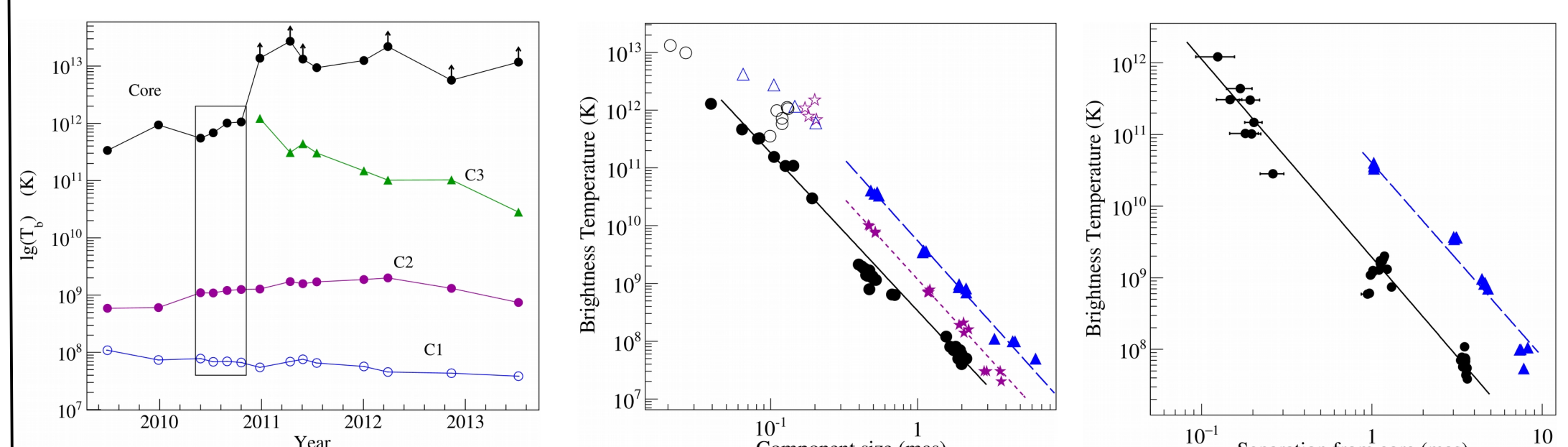- 2010-10-18

Brightness Temperature

Figure 8. Time evolution of the brightness temperature of the modeled components at 15.4 GHz at 14 VLBA epochs. The black rectangle shows four epochs of a multiwavelength monitoring campaign.

Figure 9. Brightness temperature versus size of modeled components at 15.4 GHz (black circles), 8.1 GHz (violet stars) and 4.6 GHz (blue triangles). Core components are given by empty symbols and have not been considered in the analysis. The power-law fits are shown by lines.

Figure 10. Brightness temperature versus distance from the apparent core position at 15.4 GHz (black circles) and 4.6 GHz (blue triangles). The power-law fits are shown by lines.

Brightness temperature of the 15 GHz core (given in Figure 8) is close to the equipartition value of 5×10^{10}K at $2009-06-25 - 2010-10-18$, and rises to 3×10^{11}K after 2010–10–18, when new component emerges from the core. Under an assumption of a stable conical jet with constant Lorentz factor of the emitting electrons and power-law dependences of the particle density Ne∝r^{-n}, magnetic field strength B∝r^{-b}, and jet transverse size d∝r^l for optically thin synchrotron emission (Kadler et al. 2004) the brightness temperature decreases with the distance r from the jet base and the size of the components d as $T_{b,jet} \propto r^{-f}$ and $T_{b,jet} \propto d^{-\xi}$ accordingly, where f = -l + n + b(1-α). Indexes f and ξ have been estimated from observations (Figure 9 and Figure 10) of f≈2.75 and ξ≈2.8. Considering these results, index l can be estimated as f/ξ and is close to 1.

Indexes n and b can be calculated from the core shift results, brightness temperature dependences and taking α=-0.82 from k=(3-2α)b+2n-2 / (5-2α) and f = -l + n + b(1-α). It results in n≈1.7 and b≈1.1.

15 GHz OVRO light curve decomposition

We modeled 15 GHz radio light curve as a sum of separate exponential flares (see Figure 11). We considered the fastest flare to estimate the intrinsic jet parameters, and apply these results to the fastest apparently moving component. It leads to the Lorentz factor (Γ_{var} =9.0±1.1), Doppler boosting factor (D_{var} ≈15) and the viewing angle (θ_{var} =2.7±0.6 degrees).

Applying these parameters to the core shift results, we estimate the magnetic field strength at 1 pc from the jet apex of about 1.8 G.
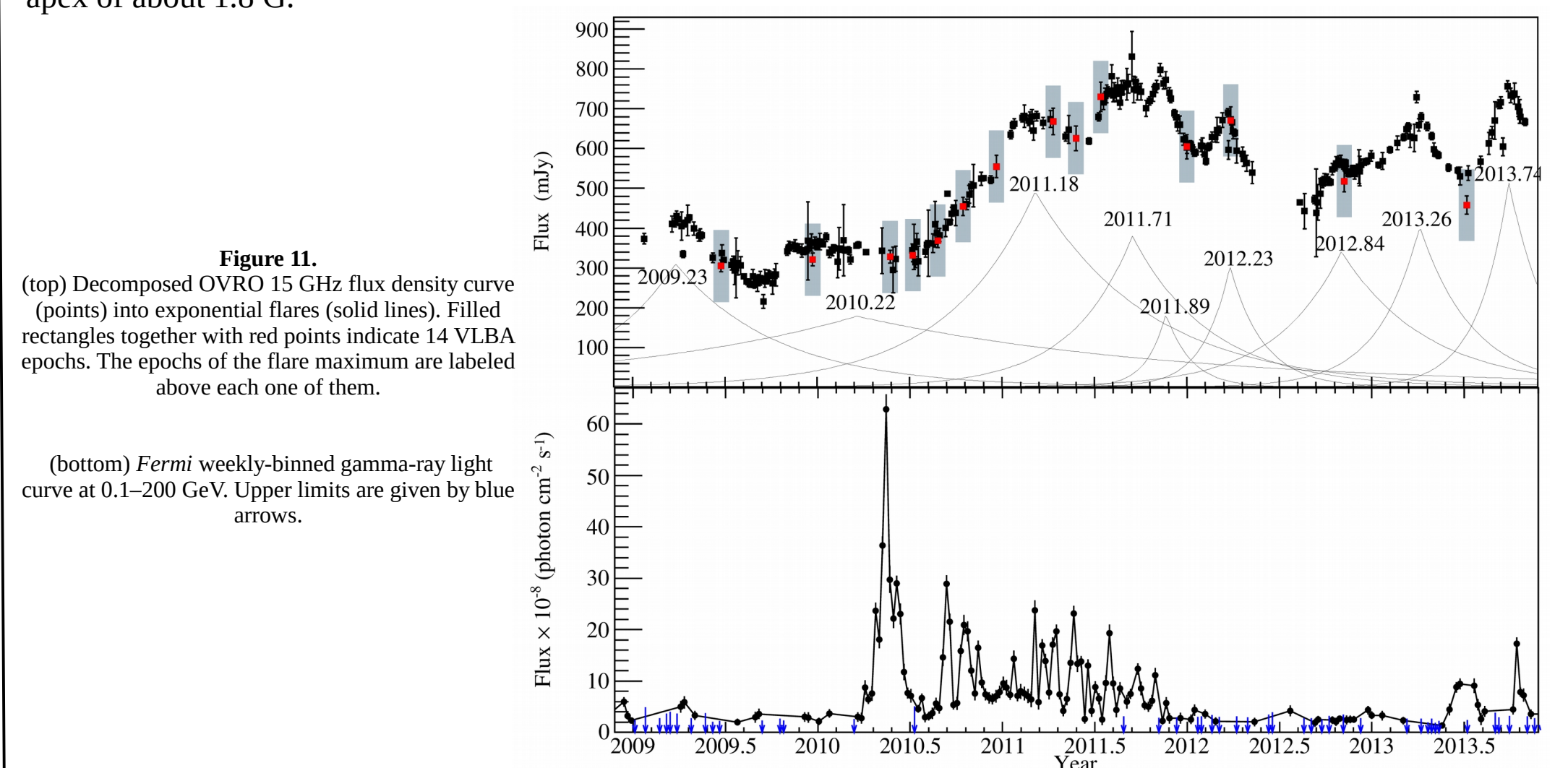
Figure 11.
(top) Decomposed OVRO 15 GHz flux density curve (points) into exponential flares (solid lines). Filled rectangles together with red points indicate 14 VLBA epochs. The epochs of the flare maximum are labeled above each one of them.

(bottom) *Fermi* weekly-binned gamma-ray light curve at 0.1–200 GeV. Upper limits are given by blue arrows.

Radio – gamma – ray connection

The correlation between the radio and gamma-ray light curves is insignificant. By visual inspection of the light curves (Figure 11) it is evident that both bands experience enhanced activity around the same time. The first and strongest gamma-ray flare peaks at 2010--04--15 and the first large radio flare during this activity period at 2011--03--07. If we assume that the events are connected, the estimate on the deprojected distance of the gamma-ray emitting region from the 15 GHz core region is of 12 pc.

Taking into account the deprojected distance of the apparent radio core from the central black hole of (14±3) pc, coming from core shift analysis, we interpret that the gamma-ray emission originates ~ 2 pc from the central engine.